International Journal of Solids and Structures 46 (2009) 1499–1515

Contents lists available at ScienceDirect

International Journal of Solids and Structures

journal homepage: www.elsevier.com/locate/ijsolstr

High strain-rate behavior of ice under uniaxial compression

Mostafa Shazly [a], Vikas Prakash [a,*], Bradley A. Lerch [b]

[a] Department of Mechanical and Aerospace Engineering, Case Western Reserve University, 10900 Euclid Avenue, Glennan 616B, Cleveland, OH 44106-7222, United States
[b] NASA-GRC, 21000 Brookpark Rd., M.S. 49-7, Cleveland, OH 44135, United States

ARTICLE INFO

Article history:
Received 13 June 2008
Received in revised form 23 October 2008
Available online 7 December 2008

Keywords:
Ice mechanics
Split Hopkinson pressure bar
High strain-rates
Uniaxial compression
Dynamic peak strength

ABSTRACT

In the present study, a modified split Hopkinson pressure bar (SHPB) is employed to investigate the dynamic response of ice under uniaxial compression in the range of strain rates from 60 to 1400 s^{-1} and at initial test temperatures of −10 and −30 °C. The compressive strength of ice shows positive strain-rate sensitivity over the range of strain rates employed; a slight influence of ice microstructure is observed, but it is much less than that reported previously for ice deformation under quasi-static loading conditions [Schulson, E.M., Iliescu, D., Frott, A., 2005. Characterization of ice for return-to-flight of the space shuttle. Part 1 – Hard ice. NASA CR-2005-213643-Part 1]. Specimen thickness, within the range studied, was found to have little or no effect on the peak (failure) strength of ice, while lowering the test temperature from −10 to −30 °C had a considerable effect, with ice behaving stronger at the lower test temperature. Moreover, unlike in the case of uniaxial quasi-static compression of ice, the effect of specimen end-constraint during the high rate compression was found to be negligible. One important result of these experiments, which may have important implications in modeling ice impacts, involves the post "peak-stress" behavior of the ice in that the ice samples do not catastrophically lose their load carrying capacity even after the attainment of peak stress during dynamic compression. This residual (tail) strength of the damaged/fragmented ice is sizable, and in some cases is larger than the quasi-static compression strength reported for ice. Moreover, this residual strength is observed to be dependent on sample thickness and the strain rate, being higher for thinner samples and at higher strain-rates during dynamic compression.

© 2008 Elsevier Ltd. All rights reserved.

1. Introduction

Since the catastrophic breakup of the Space Shuttle Columbia, NASA has been active in classifying potentially deleterious debris sources and their destructive capability due to impact. Ice has been identified as one of the potential sources of debris. Attempts to use existing models for dynamic behavior of ice have demonstrated the need for a better understanding of the response of ice at elevated strain-rates. In view of this, an experimental investigation was undertaken at Case Western Reserve University (CWRU) in close collaboration with researchers at the NASA Glenn Research Center, Cleveland, OH, to obtain the high strain-rate behavior of ice. Besides providing fundamental information on how the dynamic compressive strength of ice varies with the loading rate, the data from the present study can be used to validate and/or develop new material models for ice impact analyses, for example, understanding the severity of ice impacts on aero-frames and structures (Kim and Kedward, 2000; Kim et al., 2003), impact cratering in ice (Sherburn, 2007), to name a few.

Ice can be regarded as a class of materials rather than a single specific material with well-defined properties. Ice has thirteen different crystal structures and two amorphous states. The ice of interest in the present study is ice Ih, which has a hexagonal crystal structure and forms at ambient pressures. In the literature, Schulson (2001) has referred ice Ih as ordinary or terrestrial ice, but since it is the only form of interest here it will simply be referred to as ice.

There is a large body of existing work that describes the compressive and tensile behavior of ice (Haynes, 1978; Currier and Schulson, 1982; Dempsey et al., 1999a; Dempsey et al., 1999b; Schulson, 1999; Schulson et al., 2005), and its fracture properties (Nixon and Schulson, 1987; Weber and Nixon, 1996; Dempsey et al., 1999a; Dempsey et al., 1999b; Uchida and Kusumoto, 1999), in either single-crystal or polycrystalline forms. Most of these studies have focused on the mechanical behavior in the creep and quasi-static deformation regimes. Like many brittle materials, it is understood that ice is stronger in compression than in tension. However, unlike most brittle materials, ice is known to exhibit brittle behavior up to the melting point at strain rates that are too low for inertial confinement to play a role (Schulson, 2001). Both Schulson (2001) and Petrovic (2003), report the strength of ice is a func-

* Corresponding author. Tel.: +1 216 368 6440; fax: +1 216 368 3007.
E-mail address: vikas.prakash@case.edu (V. Prakash).

0020-7683/$ - see front matter © 2008 Elsevier Ltd. All rights reserved.
doi:10.1016/j.ijsolstr.2008.11.020

tion of grain size, and exhibits the Hall–Petch effect. It has been shown by Carter (1971) that the strength of single-crystal ice is also sensitive to the crystal orientation, and significant variations in the mechanical properties of carefully manufactured ice have been observed from batch to batch. Sample compressive strengths of ice at −10 °C have been reported by Schulson et al. (2005) to be 14.8 ± 2.3 MPa in its single-crystal form and in the range of 6.5–9.5 MPa for columnar-grained polycrystal samples. In the latter case, the compressive strength was obtained by loading ice in a direction parallel to the long axis of the grains, i.e., along the columns.

Ice exhibits a variety of behaviors in compression, ranging from ductile to brittle, as a function of strain rate. The ductile to brittle transition is understood to occur at a strain rate of $\sim 10^{-3}$ s^{-1} and at a test temperatures of −10 °C. Schulson (2001) has shown a dramatic increase in the compressive failure stress of polycrystalline ice – from 0.5 MPa at a strain rate of 10^{-8} s^{-1} to 10 MPa at a strain rate of 10^{-3} s^{-1}, and then a decline to 6 MPa at 10^{-1} s^{-1} (with considerable scatter in data). However, Cole (2001), in their study reported the failure stress of ice to be independent of the strain rate in the strain-rate range of 10^{-2}–10^{-1} s^{-1}.

At higher strain-rates, relatively few studies exist for the behavior of ice, and when they do they typically only cover the strain rates in the regime 10–100 s^{-1} (Dutta, 1993; Jones, 1997; Dutta et al., 2003; Jones, 2007). However, in events involving ice-structure interactions, such as, ice drilling/crushing and high-speed ice impacts, the strain rates in ice are much larger than those considered in the limited experimental studies on ice thus far. Moreover, results of studies conducted at strain rates of 10–100 s^{-1} (Dutta, 1993; Jones, 1997; Dutta et al., 2003) show counterintuitive results, at least based on the understanding of the strain-rate behavior of common structural materials. The studies by Dutta (1993) and Dutta et al. (2003) suggest that the strength of ice at high strain-rates is lower than that obtained in the quasi-static deformation regime (i.e., strain rates between 10^{-2} and 10^{-3} s^{-1}). The study by Jones (1997), however, does not show this trend in the behavior of ice with increasing strain-rates. In a more recent study Kim and Keune (2007) used the split Hopkinson pressure bar to study the peak strength of ice in the strain-rate range 400–2600 s^{-1}. The compressive strength of ice was observed to be essentially constant at a level of 19.7 MPa. Although results of the studies by Dutta (1993, 2003), follow the trend shown by ice at what is defined as the brittle to ductile behavior at strain rates higher than 10^{-3} s^{-1} (Schulson, 1990), they do not explain the increase in impact forces measured during the higher velocity ice impacts (St. John and Daley, 1984). Additionally, extrapolations of the quasi-static compressive strength to higher strain-rates do not provide clear trends as to whether strength of ice increases decreases or remains the same as the strain rate is increased. Moreover, past quasi-static results indicate that the compressive strength of ice is highly microstructure dependent and it is unknown whether this trend would continue in the high strain-rate regime.

Thus, in an effort to better understand the mechanical behavior of ice at elevated strain-rates, an experimental study was undertaken at CWRU in collaboration with scientists at the NASA Glenn Research Center, Cleveland, OH. In this study, the conventional split Hopkinson pressure bar (SHPB) was modified to accommodate low-temperature testing of ice at elevated strain-rates (strain-rate tests in the range of 60–1400 s^{-1} and test temperatures of −10 and −30 °C) (Shazly et al., 2005). Disk shaped ice specimens, with flat and parallel end faces, were provided by IRL, Dartmouth College, Hanover, NH, and also grown at CWRU. The effects of strain rate, sample size, test conditions, and temperature on the compressive strength of ice were systematically investigated.

2. Experimental procedures

2.1. Ice specimens

The ice specimens were either single-crystal ice provided by the IRL or polycrystalline ice samples grown at CWRU. The samples provided by IRL were machined from ice cylinders provided by Ice Culture, Inc. of Hensall, Ontario, Canada. Ice Culture Inc. grows ice for the ice sculpting industry, in a series of tanks manufactured by Clinebell Equipment Co., Inc. of Loveland, Colorado. The process consists of lining each tank with plastic sheet, filling with filtered, biologically clean water, and then freezing from the bottom up. Freezing occurs over a period of four days during which the water is stirred vigorously by two submersible pumps to remove gas bubbles from the ice–water interface. The ice that is formed is a transparent, bubble-free block, of dimensions 20 in. wide × 40 in. long × ∼8 in. thick.

The ice cylinders are harvested from the ice blocks using a computerized numerically controlled router. The cylinders used in SHPB testing were harvested by cutting directly downward so that the long axis of the cylinder was parallel to the thickness of the ice block and also the growth direction of ice, with the microstructure characterized as predominantly columnar-shaped grains. For the purposes of high strain-rate compression testing using the split Hopkinson pressure bar, disk shaped specimens were dressed to final dimensions using a milling machine. The nominal diameter of the samples was in the range of 17.5–18.5 mm. Although the specimens were not exactly cylindrical, the diameter was calculated based on the specimen weight and the measured thickness. The specimens had a thickness of 5.0–9.0 mm and the impact faces were milled parallel to within 0.076 mm. The samples were shipped from Dartmouth College to CWRU in containers packed with dry ice and stored upon arrival in a freezer at −15 °C.

The ice samples at CWRU were grown between two flat aluminum inserts, as shown in Fig. 1. The inserts were spaced at a predetermined distance and then wrapped with masking tape to form a mold. A small hole was made in the masking tape to fill the compartment between the two inserts with water. The hole also acted as a drain for water from the compartment when it froze. De-ionized sodium free water was used to make the ice samples. The whole assembly was then placed inside a freezer at the desired temperature. The ice nucleation and growth process required approximately 30 min, before the samples were taken out of the freezer for testing. Due to the high thermal conductivity of the aluminum inserts, ice crystals initiated simultaneously from the faces of the aluminum inserts and grew towards the center of the compartment. This growth process resulted in a noticeable interface at the mid-plane of the ice specimens; since the interface was nearly

Fig. 1. Photograph showing the two aluminum inserts with the ice sample in between. Disk-shaped ice samples were grown in a freezer at CWRU using this assembly.

perpendicular to the axis of the disk, its effect on the dynamic compression strength of ice was assumed to be negligible.

2.2. Microstructural examination of the ice samples

The microstructure of the Ice Culture, Inc ice and the CWRU ice was characterized at Dartmouth College. In the case of the Ice Culture ice, the ice cylinders were initially screened using crossed polarizing-filters, and were determined to be sufficiently transparent to allow the unaided eye to detect individual grains in different shades of grey. Subsequently, thin sections (~1 mm thick) from end-cuts of some of the cylinders were prepared for more careful observation of the microstructure, through cross-polarizers.

The micro-structural analysis revealed that on an average the Ice Culture blocks possessed a columnar-grained microstructure with grain diameters ranging from 6 to 7 mm in samples from near the bottom of the blocks to 9–10 mm in samples from near the top. However, certain regions from within a given ice block comprised of grains several times larger than average, owing perhaps to slower freezing rates. As a result, small (17–50 mm) diameter cylinders, harvested randomly from a given block, occasionally contained only one or two grains. Thus, while selecting specimens for mechanical testing care was taken to ensure microstructure similarity.

Besides microstructure, thin sections of some cylinders were used to determine the orientation of the crystallographic *c*-axis. Terrestial ice possesses hexagonal symmetry, and the *c*-axis is defined as the normal to the basal plane of a unit cell. In order to establish the orientation of the ice samples a four-axis stage (Rigsby, 1951) was employed. It was determined that on an average the angle of the *c*-axis relative to the axis of the parent cylinder was between 80° and 85°. This implies that the ice possessed a strong crystallographic texture that did not vary significantly from either block to block or within a give block. This is important since it has been previously shown (Shan et al., 2000) that under quasi-static compression loading the orientation of the single-crystal ice can affect the strength of ice by as much as a factor of 3.

For the purposes of high strain-rate testing, the microstructure of the ice supplied by IRL was essentially a single crystal but contained a lot of sub-grain boundaries. Fig. 2 shows the birefringent pattern of a representative disk providing evidence that the samples were essentially single crystalline.

On the other hand, as shown in Fig. 3, the ice samples grown at CWRU were multi-grain structures. Ice crystals preferentially nucleate from the aluminum inserts, creating small equiaxed grains up to 1.5 mm in diameter. As freezing continues, grains grow from the two sides with final freezing occurring at the mid-plane. The resulting grains are large – being approximately 3 mm in diameter by 5 mm in length for the longest grains. Transverse sections (Fig. 3(b)) indicate that the large grains have an extensive substructure.

2.3. Low-temperature split Hopkinson pressure bar facility

A SHPB was employed to conduct the high strain-rate compression tests. The schematic of the SHPB facility is shown in Fig. 4. The facility comprises a striker bar, an incident bar and a transmitter bar, all made from 19.05 mm diameter high-strength 7075-T6 Al alloy having a nominal yield strength of 500 MPa. Striker bars with lengths of 75 and 152 mm were used in the present study. The incident and transmitter bars were approximately 1.8 m long. The striker bar is accelerated using an air operated gas gun. A pair of semiconductor strain gages (BLH SPB3-18-100-U1) are strategically attached on the incident and transmitter bars and are used in combination with a Wheatstone bridge circuit connected with a differential amplifier (Tektronix 5A22N) and a digital oscilloscope (Tektronix TDS 420) to monitor the strain pulses during the test. The impact velocity of the striker bar was varied between 2 and 14 m/s so as to obtain strain rates in the range 60–1400 s^{-1}. In order to better understand the failure process of ice, a high-speed camera, Hadland IMACON 200, with a maximum framing rate capability of 200 million frames per second was used to image the failure process.

In a typical SHPB test, a compressed-air gas gun is used to accelerate the striker bar and impact the incident bar at a pre-determined velocity. The impact results in an elastic compression wave, with a strain profile $\varepsilon_i(t)$, to travel in the incident bar towards the specimen. Due to the impedance mismatch between the specimen and the pressure bars, part of the incident compressive wave is reflected back into the incident bar, and is denoted by $\varepsilon_r(t)$, while the rest, denoted by $\varepsilon_t(t)$, is transmitted through the specimen into transmitter bar. Under the assumption of homogeneous deformation, elementary 1D elastic wave-propagation is used to calculate the engineering stress $\sigma_s(t)$, the strain rate $\dot{\varepsilon}_s(t)$, and strain $\varepsilon_s(t)$ in specimen as

$$\sigma_s(t) = E\frac{A_0}{A_s}\varepsilon_t(t), \tag{1}$$

$$\dot{\varepsilon}_s(t) = -2\frac{c_0}{L_s}\varepsilon_r(t), \tag{2}$$

$$\varepsilon_s(t) = \int_0^t \dot{\varepsilon}_s(t)dt. \tag{3}$$

In Eqs. (1)–(3), E, A_0, and c_0 are Young's modulus, cross-sectional area, and longitudinal wave speed in pressure bars, respectively, while A_s and L_s are the initial cross-sectional area and length of the specimen, respectively. The true stress- and strain-rate are determined from the engineering stress- and strain-rate by assuming uniform and isochoric deformation conditions to prevail within the specimen during the deformation process.

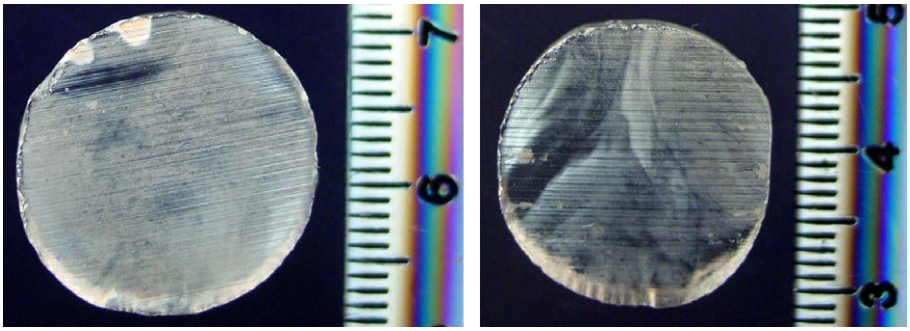

Fig. 2. Single-crystal ice specimen obtained from IRL at Dartmouth College (Scale in mm).

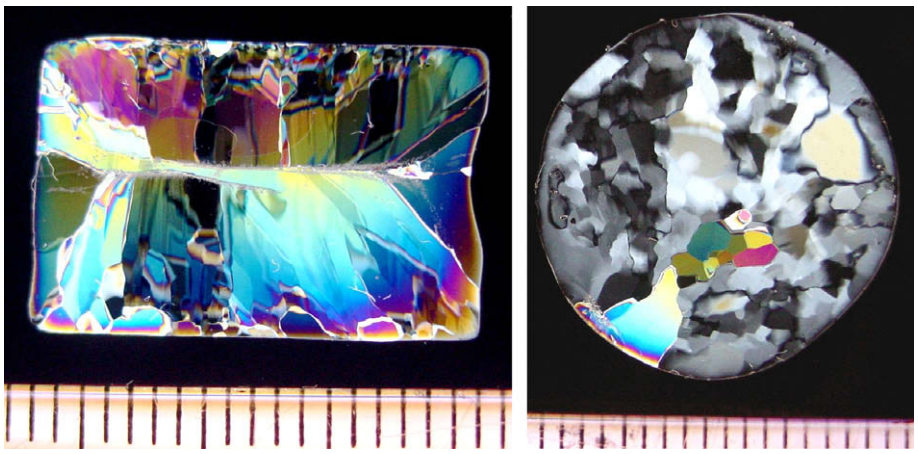

Fig. 3. Typical microstructure of CWRU's ice samples. (a) Longitudinal section and (b) transverse section. Please note the vertical lines represent the scale; the spacing between the lines is 1 mm.

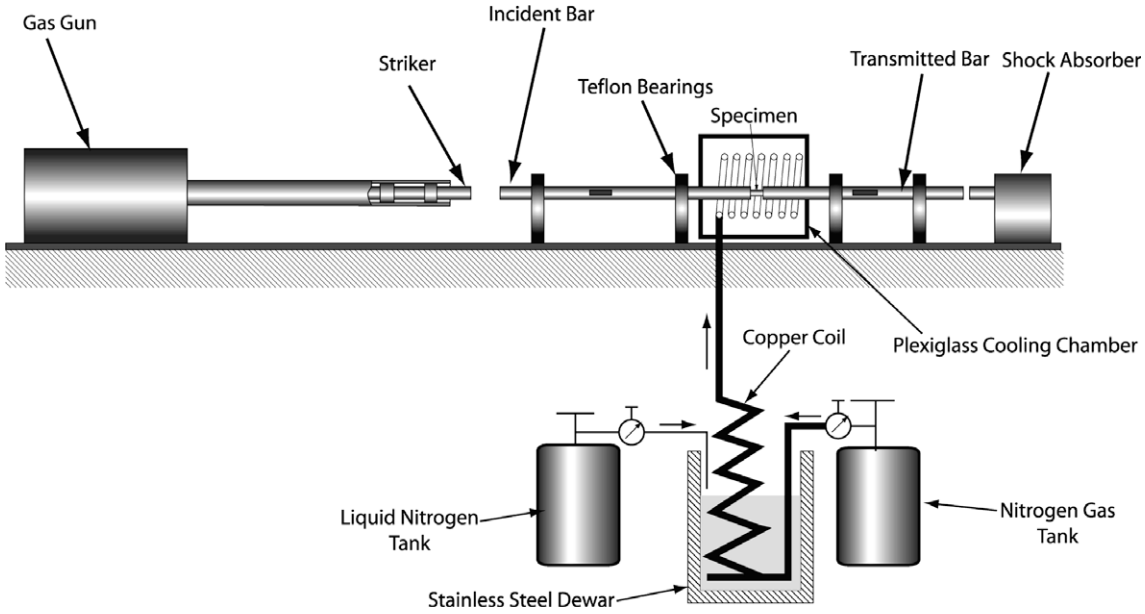

Fig. 4. Low-temperature split Hopkinson pressure bar facility at the Case Western Reserve University.

In order to conduct the low-temperature experiments, a cooling chamber was designed and built around the specimen. The chamber was built from Plexiglas plates having a thickness of 31.75 mm to maximize insulation efficiency and maintain the sub-zero temperatures in the chamber. A 3/8″ standard copper tube was shaped in a coil form and immersed in liquid nitrogen in a Dewar. One end of the coil was connected to a nitrogen gas or air tank while the other end is shaped into a larger coil to surround the SHPB bars and the ice specimen in the cooling chamber. The coil carries the cooled air to the cooling chamber and helps to maintain it at the desired sub-ambient temperatures. The temperature inside the chamber was monitored by a 0.015″ diameter chromel–alumel wire placed in close proximity to the specimen. Circulation of the cooled air within the cooling-chamber helps to maintain a uniform temperature. The test temperatures used in the present study were −10 and −30 °C.

For experiments performed on pre-machined single-crystal ice specimens, the specimen was placed between two aluminum inserts of the same material and diameter as the SHPB bars. The assembly of the ice disk and the inserts was transported from the freezer to the test rig in a cryo-container. A thin layer of vacuum grease was used between the ice specimen and the inserts in order to minimize friction, and hence the end-constraint during testing, and also to hold the ice sample in place between the SHPB bars.

2.4. Pulse shaping and nearly constant strain-rate experiments

Based on the available literature (Petrovic, 2003) ice has an average Young's modulus of 10 GPa and an approximate density of 1000 kg/m^3. These values give a longitudinal elastic wave speed of 3162 m/s in ice. As pointed out by Davies and Hunter (1963), in a typical split Hopkinson bar test the stress state within the specimen equilibrates after approximately π reverberations of the stress pulse within the specimen, i.e.,

$$t_{equil} = \frac{\pi L_0}{c_{ice}}, \tag{4}$$

where L_0 is the specimen length and c_{ice} is the longitudinal wave speed in ice.

In view of Eq. (4), for the experiments conducted in the present study, the stress in the 8-, 5-, and the 2.3-mm-thick ice specimens are expected to reach an equilibrium after approximately 8, 5, and 2.3 μs, respectively. In this way, the times for attainment of peak stress in the ice specimens is always greater than those required to reach an equilibrium state of stress in the specimens. This condition can be facilitated by using proper pulse shapers to shape (increase) the rise time of the incident pulse. In view of this, in the present study, annealed copper shims of various sizes were used as the pulse shapers (Frew et al., 2002). These copper shims were placed on the impact (left) end of the incident bar, and thus, get sandwiched between striker and the incident bars during impact. The size of the shim was determined by trial and error depending on the impact velocity and the type of ice being tested. In the first trial, a test was run with an arbitrary pulse shaper size. The transmitted signal was then used to optimize the pulse shaper by matching the slopes of the incident signals (resulting from impacting the incident bar with different pulse shapers placed between the incident and striker bars) with the transmitted signal of the first test.

Fig. 5 shows results of experiments conducted to optimize the size of the pulse shaper for impact velocities of 2.6 and 5 m/s. In Fig. 5(a), an initial trial on a $3 \times 3 \times 0.25$ mm pulse shaper showed that the slope of the input signal is lower than the transmitted signal. Incremental increases in the pulse shaper dimensions (keeping the same thickness) were performed to increase the longitudinal impedance of the pulse shaper, to make it stiffer, and also to reduce the magnitude of plastic-flow upon impact. Two sets of experiments were performed at the larger dimensions to assure such a behavior. For the case of the higher impact velocity, a thinner pulse shaper of 0.13 mm was the first choice as it is expected to show less plastic flow, and thus a steeper input signal should be obtained. This trial experiment was unsuccessful and the previous thickness of 0.25 mm was then used but with larger lateral dimensions. Similarly, two trials were performed for the same dimensions for verification. It is clearly shown in Fig. 5(b) that for a given pulse shaper material the required dimensions for the pulse shaper depend on the impact speed.

Since ice is a brittle material (particularly in the ranges of temperatures and strain rates of interest in the present study), the failure strains are less than 1%. Since the strain rate starts at zero in the beginning of the test and must increase during loading, there is little time to establish a constant strain-rate before the samples fail. Achieving a degree of constant strain-rate loading was maximized through the use of pulse shapers. The average strain-rate listed in the tables represents an average value taken near the maximum load (i.e., at fracture). The strain rate can vary by as much as 200 s^{-1} during this time. Nonetheless, given the small fracture strains in ice, this is the best that could be achieved. Similar difficulties have been observed in other brittle materials such as Zr-based bulk metallic glass (Sunny et al., 2007), ceramics (Sarva and Nemat-Nasser, 2001) and rocks during their high strain-rate testing using the split Hopkinson pressure bar (Shan et al., 2000).

3. Experimental results

In the present study four series of high strain-rate experiments were conducted using the low-temperature split Hopkinson pressure bar. The ice samples for these tests were supplied by IRL and/or grown at CWRU. The results from the four series of experiments are described in the following. Interested readers are also referred to a comprehensive NASA technical report (Shazly et al., 2006), which provides further details of the present experimental study.

3.1. Dynamic compression of single-crystal ice specimens at a test temperature of −10 °C

The first series of experiments was conducted on single-crystal ice specimens obtained from IRL, and will be referred to as the 6-SX series of experiments. The specimens were approximately 18 mm in diameter and 5.5 mm in thickness. The test temperature was −10 °C. In order to minimize friction between the specimen and the loading face of the striker and the transmitter bar, vacuum grease was used at the specimen–bar interface. High-speed photography was used in select experiments. Tables 1 and 2 summarize the experimental parameters and results for this set of experiments, respectively.

Fig. 6 summarizes the true stress versus strain behavior on the single-crystal ice samples at −10 °C. A striker bar of length 150 mm was employed in all experiments except for experiments 6SX-8 and 6SX-12, where a shorter striker bar of length 75 mm was used. By employing proper pulse shaping a near constant strain-rate was achieved in the specimens during the dynamic compression process. For the relatively lower impact velocity experiments, i.e., experiments 6SX-4, 6SX-7, 6SX-8, and 6SX-9, the strain rates in the specimens were in the range of 90–460 s^{-1}. The corresponding peak stress levels in the specimen were in the range 20–24 MPa. These peak strength levels are markedly higher when compared to those reported in literature for ice under quasi-static deformation conditions. At the higher impact velocities the peak stresses are even higher. In all cases no evidence of catastrophic stress drop was observed in the transmitted strain-gage signal after the attainment of peak stress; the peak stress, after an initial softening was followed by a relatively long tail indicating that stress was still carried by the pulverized/fragmented ice. For the shorter length striker-bar, the strain accumulated in the ice specimen was less than the failure strain, and consequently the specimen in experiment 6SX-8 did not yield or fail during the loading pulse, and significant elastic recovery is evident in Fig. 6. The peak stress is followed by a relatively large tail. This relatively long tail can perhaps be explained by considering the damaged/fragmented ice as an assemblage of granular material. In this way, the residual strength of ice, after the initial damage, can be attributed to the relatively high inter-granular friction due to the complex geometry of the ice fragments, which could potentially significantly increase the resistance to flow of the damaged/fragmented ice. It is also possible that at the high loading rates used in the experiments, localized adiabatic heating at various interfaces in the fragmented ice may result in local melting, thus increasing the cohesive strength of the various fragmented pieces in the damaged ice.

High-speed photography was employed in selected experiments, i.e., 6SX-4, 6SX-9, and 6SX-11, to better understand the deformation and failure processes in the ice samples. The first evidence of cracking was observed in frames corresponding to loads being close to their peak levels. After attainment of the peak stress a large number of axial cracks were observed in the sample. The number of these microcracks was observed to increase as the deformation proceeded, eventually leading to complete fragmentation of the specimen. The stress versus strain profile from one such experiment (6SX-3), from the first series of experiments, are shown in Fig. 7. A nominally constant strain-rate of 882 s^{-1} was achieved in the experiment. The first evidence of cracking in the sample is observed in Frame 5 in Fig. 7(b), with the stress level close to its peak stress.

3.2. Dynamic compression ofCWRU-grown-polycrystalline ice at a test temperature of −10 °C

The second series of experiments, also referred to as the HMD-series, was conducted on ice samples grown at CWRU. These ice

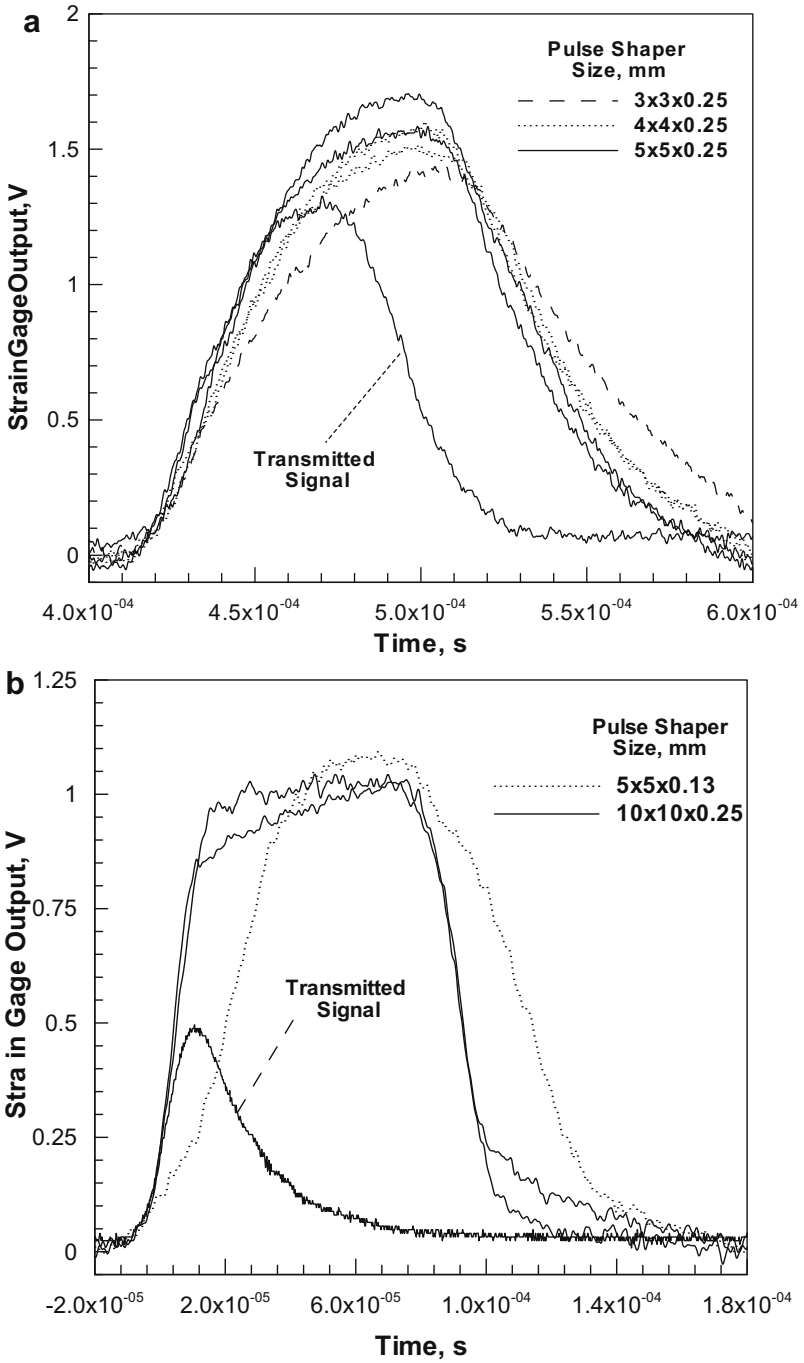

Fig. 5. Pulse shaper optimization by trial and error method to match the slopes of the incident and transmitted signals for impact velocities of (a) 2.6 and (b) 5.0 m/s.

Table 1
Experimental parameters for 6SX experiment series on single-crystal ice supplied by IRL.

Test number	Specimen dimensions		Chamber temperature (°C)	Striker bar length (mm)	Pulse shaper size (mm)
	Diameter (mm)	Length (mm)			
6SX-3	18.62	5.49	−11.3	76.2	10 × 10 × 0.25
6SX-4	18.49	5.36	−11.0	152.4	No shaper
6SX-6	18.42	5.77	−11.4	152.4	10 × 10 × 0.25
6SX-7	18.52	5.26	−9.3	152.4	10 × 10 × 0.25
6SX-8	18.39	5.54	−12.1	152.4	10 × 10 × 0.25
6SX-9	18.37	5.38	−11.0	152.4	5 × 5 × 0.25
6SX-11	18.31	5.46	−12.0	152.4	9 × 9 × 0.25
6SX-12	18.38	5.05	−11.0	76.2	10 × 10 × 0.25

Table 2
Experimental results for 6SX experiment series on single-crystal ice supplied by IRL.

Test number	Striker bar velocity (m/s)	Average strain-rate (s^{-1})	Peak stress (MPa)	Strain at peak stress ($\times 10^{-3}$)	Time at peak stress (μs)
6SX-3	10.0	882	33.5	8.3	21.7
6SX-4	2.9	130	20.7	5.0	56.5
6SX-6	4.8	260	24.8	7.8	39.7
6SX-7	4.6	460	22.0	5.9	30.0
6SX-8	4.8	425	26.7	4.0	23.3
6SX-9	3.8	90	23.4	6.5	84.4
6SX-11	5.8	611	23.7	6.4	23.4
6SX-12	14.3	1122	34.7	7.7	15.7

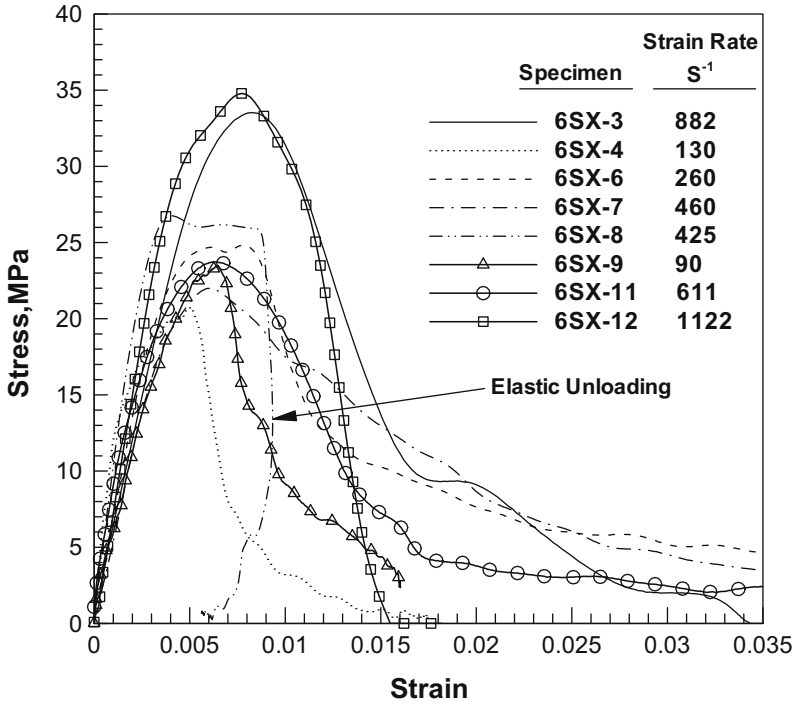

Fig. 6. Stress–strain curves at different strain rates for single-crystal ice 6SX experiment series.

samples were polycrystalline when compared to the samples used in the first series of experiments, which were single crystal. The test conditions for this series of experiments are similar to those employed for the 6-SX series, except that no vacuum grease was used at the specimen–insert interface. In the 6-SX series, for the highest strain-rate experiments the peak stress (failure stress) was attained at a time comparable to the stress equilibrium time. Therefore, in order to attain higher strain-rates with failure times greater than the corresponding equilibrium times, thinner specimens than those used in the 6SX series of experiments were employed. The thinner samples are expected to reach stress equilibrium at much shorter times, and thus provide more reliable evaluation of the peak stress at failure. Three different sample thicknesses of 5.5, 2.3, and 0.89 mm were tested at the test temperature of −10 °C. High-speed photography, with an inter-frame time of either 5 or 8 μs, was employed in a few select experiments.

Table 3 summarizes the experimental parameters, while Table 4 summarizes the experimental results for this series of experiments. In this series of experiments, the onset of cracking is observed to occur close to the peak stress level. This behavior is similar to that observed for the case of the 6SX series of experiments at comparable impact speeds. Cracking was evident in high-speed photographs for experiments HMD016, HMD010, HMD011, and HMD018, respectively, while no cracking was observed for experiment HMD008. For the thinner 2.3-mm specimens, multiple cracks were seen to propagate simultaneously. This is in contrast with the single cracks that form in the thicker 5.5-mm samples.

The results of the high strain-rate tests conducted in the second series of experiments are shown in Figs. 8–10. In all cases, except for experiments HMD008 and HMD027, the ice specimens were observed to fracture; in the case of experiments HMD008 and HMD027 elastic unloading is observed. For comparison, the average failure strain (corresponding to the peak stress) for both single and polycrystalline ice under static loads was approximately $3 \pm 0.5 \times 10^{-3}$ (Schulson et al., 2005). The strain at peak stress in the present experiments is observed to increase as the specimen thickness decreases, as shown in Table 4. The average strain at peak stress for specimens with 5.5, 2.3, and 0.89 mm thickness were $5.42 \pm 3.73 \times 10^{-3}$, $8.04 \pm 1.94 \times 10^{-3}$, and $25.6 \pm 7.8 \times 10^{-3}$, respectively. It should be noted that the magnitude for the strains at failure for the 5.5 mm thick specimens are comparable to those obtained for the single-crystal ice specimens (6SX) with the same specimen thickness. Moreover, as was seen in the first series of experiments, the peak stress in the polycrystalline ice samples increases with an increase in strain rate. The stress versus strain profiles again exhibit a long tail after the attainment of peak stress, which approaches some sizable stress level as the sample thickness decreases and the strain rate increases, e.g., 10 MPa for 0.89 mm thickness at 740 s^{-1}; Fig. 10. Note that 10 MPa is the approximate

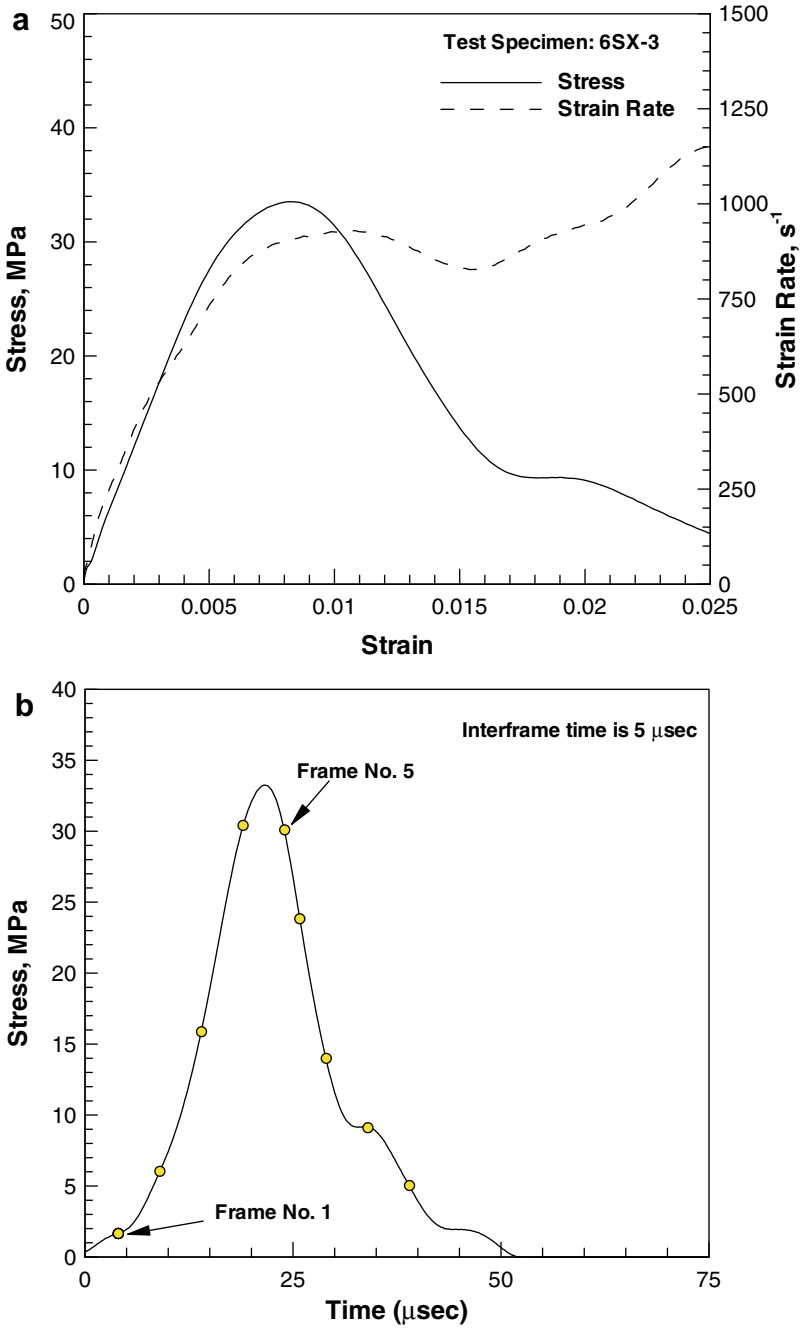

Fig. 7. (a) Stress- and strain-rate vs. strain profiles for a representative experiment, 6SX-3, on single-crystal ice at −10 °C; and (b) stress vs. time profile for the experiment, with individual frames indicated, verifying cracking near the peak stress.

compression strength of hard ice under quasi-static loading (Schulson et al., 2005).

3.3. Dynamic compression of CWRU-grown-polycrystalline ice at a test temperature of −30 °C

Previous studies on ice have shown the peak strength of ice to be temperature dependent (Haynes, 1978; Currier and Schulson, 1982; Nixon and Schulson, 1987; Weber and Nixon, 1996; Dempsey et al., 1999a; Dempsey et al., 1999b; Schulson, 1999; Uchida and Kusumoto, 1999; Schulson et al., 2005). However, at elevated strain-rates the peak stress has been reported to be temperature independent (Dutta et al., 2003). In the present study, a series of the high strain-rate tests were conducted at test temperature of −30 °C on polycrystalline samples ice grown at CWRU. Specimens with thicknesses of 5.8, 2.3, and 0.89 mm were evaluated. The experimental parameters for this set of experiments are summarized in Table 5, while the experimental results are summarized in Table 6.

Figs. 11–13 show the stress–strain behavior for the series of experiments conducted at −30 °C. While all other specimens that were evaluated failed during the tests, specimens utilized in Tests 1 and 16 did not fail as evident by the elastic unloading curves. Once again the peak stress levels are observed to have a positive correlation with strain rate. Also, specimens with 0.89 mm thickness show a distinct post failure plateau in the true stress versus strain curves and maintain a stress level as high as 20 MPa in the post peak-stress strain regime, as shown in Fig. 13. The average

Table 3
Experimental parameters for the HMD experiment series on polycrystalline ice grown at CWRU. The specimen diameter was approximately 19 mm and the striker bar length was 152.4 mm for each test.

Test number	Specimen length (mm)	Chamber temperature (°C)	Pulse shaper size (mm)
HMD003	5.5	−9.8	9 × 9 × 0.25
HMD006	5.5	−10.0	No shaper
HMD008	5.5	−11.0	No shaper
HMD016	5.5	−12.2	5 × 5 × 0.25
HMD010	2.3	−10.2	No shaper
HMD011	2.3	−11.5	5 × 5 × 0.25
HMD014	2.3	−9.7	5 × 5 × 0.25
HMD018	2.3	−10.0	No shaper
HMD019	2.3	−9.0	5 × 5 × 0.25
HMD022	0.89	−11.0	5 × 5 × 0.25
HMD024	0.89	−10.1	5 × 5 × 0.25
HMD027	0.89	−10.1	5 × 5 × 0.25

strain at the peak stress for the specimens with a 5.8 mm thickness was $6.10 \pm 1.67 \times 10^{-3}$, for specimens with 2.3 mm thickness was $10.33 \pm 1.87 \times 10^{-3}$, and for specimens with 0.89 mm thickness was $38.17 \pm 9.15 \times 10^{-3}$. These strain values are slightly higher when compared with the same specimen thickness samples tested at −10 °C, which were $5.42 \pm 3.73 \times 10^{-3}$ for specimens with a 5.5 mm thickness, $8.04 \pm 1.94 \times 10^{-3}$ for specimens with a 2.3 mm thickness, and $25.6 \pm 7.8 \times 10^{-3}$ for specimens with a 0.89 mm thickness. Again the times corresponding to the peak stress are longer than the equilibrium times, and comparable to those for the specimens tested at −10 °C. The most important observation is that the peak stresses attained for samples tested at −30 °C are higher than for specimens tested at −10 °C (compare Figs. 11–13 with Figs. 8–10).

3.4. Dynamic compression of single-crystal ice at test temperature of −10 °C in the presence of end-constraint

The fourth series of experiments were conducted to evaluate the effect of end-constraint on the measured dynamic failure strength (peak stress) of ice. In particular, the motivation for this series of experiments was to investigate whether a constrained-end condition can play a role in elevating the peak stress of the ice with an increase in strain rate. In this series of experiments sin-

Table 4
Experimental results for the HMD experiment series on polycrystalline ice grown at CWRU.

Test number	Striker bar velocity (m/s)	Average strain-rate (s^{-1})	Peak stress (MPa)	Strain at peak stress ($\times 10^{-3}$)	Time at peak stress (μs)
HMD003	6.0	770	22.7	10.9	27.7
HMD006	2.2	140	9.5	2.5	36.0
HMD008	2.0	92	11.7	4.1	59.5
HMD016	4.4	180	17.8	4.2	43.1
HMD010	2.3	312	14.6	11.1	53.0
HMD011	4.5	225	23.0	8.1	44.0
HMD014	7.4	740	23.5	6.2	21.6
HMD018	2.6	408	13.2	8.3	35.0
HMD019	4.6	397	15.1	6.5	28.7
HMD022	4.4	672	26.1	30.5	57.8
HMD024	4.5	740	22.0	16.6	33.0
HMD027	4.3	550	29.0	29.7	82.0

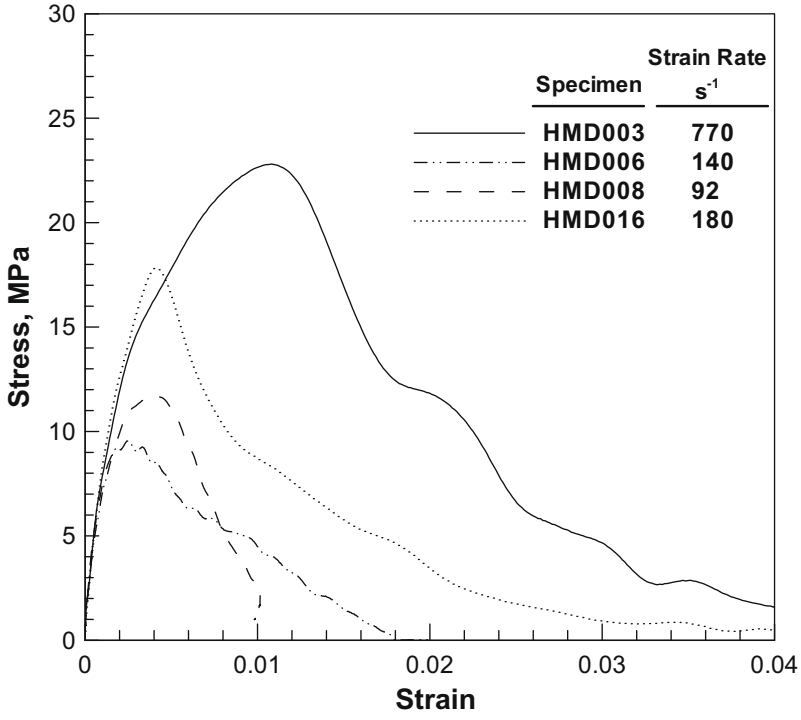

Fig. 8. Stress–strain curves at different strain rates for HMD experiments series for 5.5 mm thick polycrystalline ice samples.

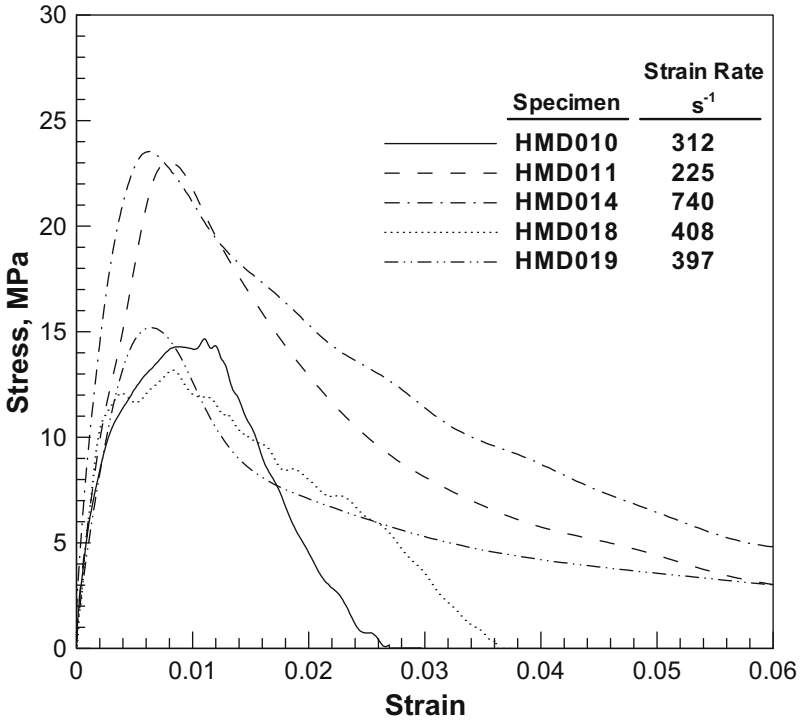

Fig. 9. Stress–strain curves at different strain rates for HMD experiments series for 2.3 mm thick polycrystalline ice samples.

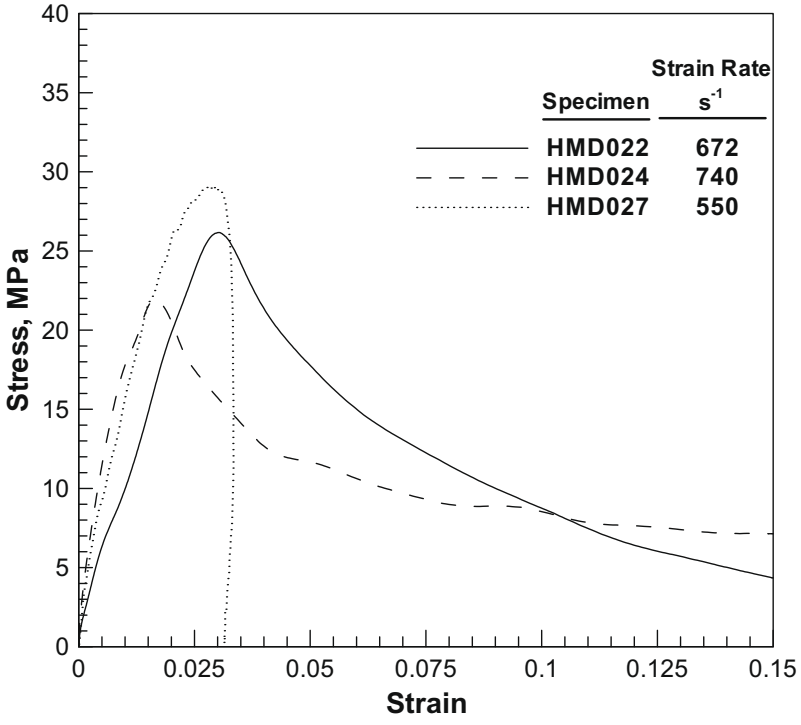

Fig. 10. Stress–strain curves at different strain rates for HMD experiments series for 0.89 mm thick polycrystalline ice samples.

gle-crystal ice specimens (14SX series), supplied by Ice Research Laboratory at Dartmouth College were utilized. In order to create relatively strong end-constraint conditions, a thin layer of water was sprayed on pre-cooled aluminum inserts, and the ice sample was set on this layer. The assembly was then kept in the freezer for at least ten minutes to allow the ice specimen to freeze to the inserts. These specimens with ends frozen to the aluminum inserts were then tested in the SHPB at strain rates similar to those employed in the previous experiments having less end-constraint (with vacuum grease). The experimental parameters for this set of tests are summarized in Table 7, while the experimental results are summarized in Table 8.

Table 5
Experimental parameters for the third series of experiments on polycrystalline ice grown at CWRU. The test temperature is ~−30 °C in all tests. The specimen diameter was approximately 19 mm for each test. The striker bar length was 152.4 mm for each test.

Test number	Specimen length (mm)	Chamber temperature (°C)	Pulse shaper size (mm)
1	5.5	−30.0	5 × 5 × 0.25
5	5.5	−28.7	11 × 11 × 0.25
6	5.5	−33.8	12 × 12 × 0.25
8	5.5	−31.8	12 × 12 × 0.25
9	2.3	−31.9	13 × 13 × 0.25
10	2.3	−30.0	13 × 13 × 0.25
11	2.3	−29.7	11 × 11 × 0.25
12	2.3	−32.9	11 × 11 × 0.25
14	2.3	−31.7	13 × 13 × 0.25
16	0.89	−33.0	11 × 11 × 0.25
17	0.89	−33.0	12 × 12 × 0.25
19	0.89	−30.0	12 × 12 × 0.25
20	0.89	−32.0	12 × 12 × 0.25

Fig. 14 shows the stress–strain diagrams for this series of experiments. The strain at the peak stress for the constrained-end condition is observed to be somewhat less than that obtained for single-crystal ice specimens (6SX) tested with the unconstrained end condition. Moreover, the times at which the peak stress occurs are greater than those observed in the case of the 6SX series. However, the peak stress levels are nearly the same in the two cases.

4. Summary of results and discussion

In the present study a modified split Hopkinson pressure bar apparatus is employed to investigate the high strain-rate behavior of ice. The compressive strength of ice was shown to have positive strain-rate sensitivity in the strain-rate range 60–1400 s^{-1}. Specimen thickness, within the range studied, was found to have little or no effect on the peak (failure) strength while the test temperature was observed to have a strong effect on the peak strength, with ice behaving stronger as the test temperature was decreased

Table 6
Experimental results for the third series of experiments on polycrystalline ice grown at CWRU. The test temperature is ~−30 °C in all tests.

Test number	Striker bar velocity (m/s)	Average strain-rate (s^{-1})	Peak stress (MPa)	Strain at peak stress ($\times 10^{-3}$)	Time at peak stress (μs)
1	4.1	62	23	6.0	83.0
5	7.0	209	39.4	8.8	45.0
6	7.0	290	35.4	5.1	24.3
8	6.8	214	36.8	6.8	39.4
9	8.9	426	31.7	3.8	22.6
10	10.0	580	34	6.1	20.3
11	7.2	323	38.4	11.1	40.1
12	6.8	250	39.6	8.2	44.4
14	7.4	502	36	11.7	28.0
16	7.4	596	44.3	46.5	43.4
17	9.3	978	54	40.7	49.1
19	8.7	842	53.7	40.4	61.4
20	10.0	1441	58.4	25.1	25.4

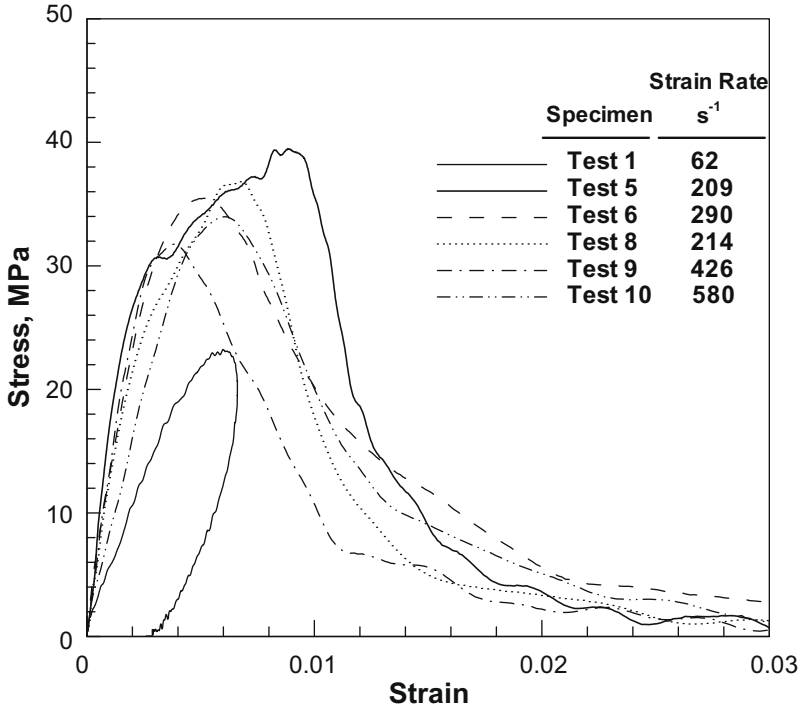

Fig. 11. Stress–strain curves at different strain rates for experiments series performed at −30 °C with 5.8 mm thick polycrystalline samples grown at CWRU.

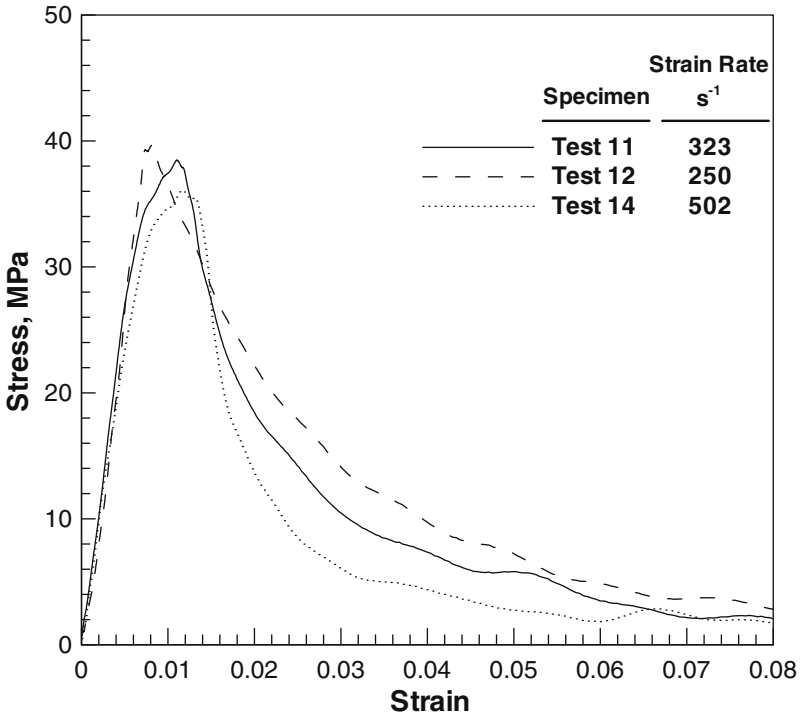

Fig. 12. Stress–strain curves at different strain rates for experiments series performed at −30 °C with 2.3 mm thick polycrystalline samples grown at CWRU.

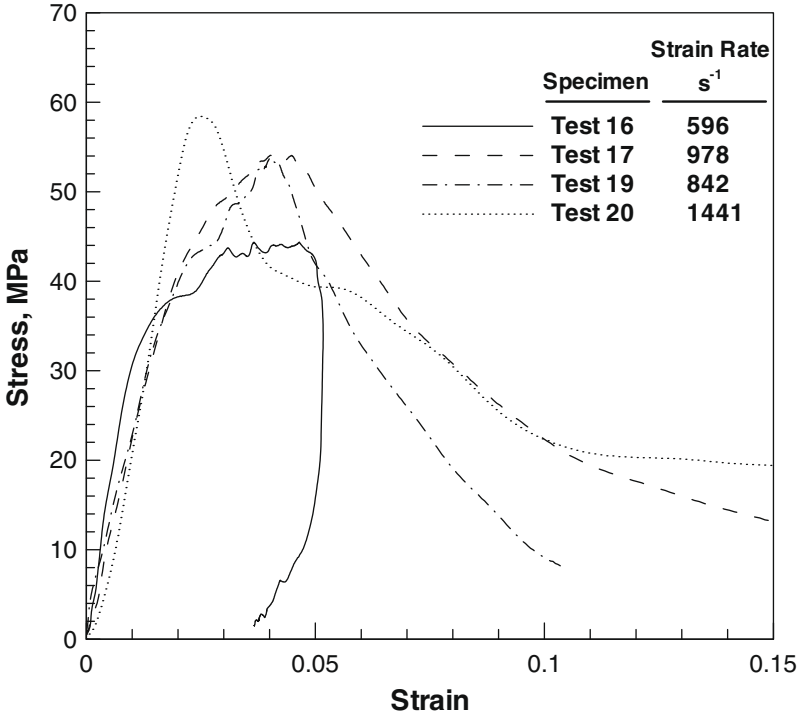

Fig. 13. Stress–strain curves at different strain rates for experiments series performed at −30 °C with 0.89 mm thick polycrystalline samples grown at CWRU.

from −10 to −30 °C. These results are in contradiction to previous high strain-rate investigations, where ice was reported to show a negative strain-rate sensitivity at strain rates of 10 s^{-1} and higher. The effect of specimen end-constraint during the high rate compression of ice was found to be negligible. Again, these results are contrary to those obtained at quasi-static loading rates where the specimen end-constraint has been shown to have a significant effect on the measured stress strain behavior.

The experimental results for peak stress as a function of the average strain-rate in the sample and the strain at peak stress as a function of the specimen thickness are summarized in Figs. 15 and 16, respectively. From Fig. 15, it is clear that the peak stress for both single-crystal and the CWRU-grown-polycrystalline ice show positive strain-rate dependency. This behavior is contradictory to other SHPB data available in the literature (Dutta, 1993; Dutta et al., 2003) in the strain-rate range 10–100 s^{-1}; however,

it correlates well with data obtained from lower strain-rate testing on servo-hydraulic machines at strain rates up to 10 s^{-1} (Jones, 1997). This behavior of positive strain-rate dependency is similar to other brittle materials such as ceramics and rocks. For example, Macor glass ceramic (Corning Inc., Corning, NY) showed a positive strain-rate dependency over a wide range of strain rates from 10^{-6} to 3000 s^{-1} (Chen, 1995), silicon carbide showed the positive strain-rate dependency at strain rates higher than 250 s^{-1} (Sarva and Nemat-Nasser, 2001), and granite showed the same behavior over strain rate range of 100–600 s^{-1}(Shan et al., 2000). Moreover, as seen from Fig. 15, no clear evidence of specimen thickness effects on the peak (failure) strength can be deduced from the experimental results, but rather there is a specimen thickness effect on the strain at peak stress as shown in Fig. 16. The peak stress reported in the work by Dutta et al. (2003, 2004) was 6.53 ± 1.44 and 6.77 ± 3.23 MPa at −10 °C under quasi-static and dynamic loading conditions, respectively. These values are two to three times lower than those obtained in the present study. It must be noted that the specimens used in the study by Dutta et al. (2003) had a length of 76 mm, which as per the analysis presented in Davies and Hunter (1963) requires about 75 μs to achieve dynamic stress equilibrium. However, the representative strain gage signals show a failure time of approximately 80 μs, which is close to the time required for the specimens to reach stress equilibrium in the 76 mm in length ice samples. Unfortunately, representative stress- and strain-rate versus strain diagrams were not provided

Table 7
Experimental parameters for 14SX experiment series on single-crystal ice samples supplied by IRL. The length of the striker bar was 152.4 mm in all tests.

Test number	Specimen dimensions		Chamber temperature (°C)	*c*-axis orientation with respect to the vertical (°)	Pulse shaper size (mm)
	Diameter (mm)	Length (mm)			
14SX-02	17.46	5.66	−11.5	50	5 × 5 × 0.25
14SX-03	17.46	5.74	−10.3	45	5 × 5 × 0.25
14SX-06	17.46	5.74	−10.3	40	5 × 5 × 0.25
14SX-07	19.0	5.89	−10.0	47	5 × 5 × 0.25
14SX-09	19.0	5.92	−10.5	45	9 × 9 × 0.25
14SX-18	19.0	8.69	−11.0	0	5 × 5 × 0.25

Table 8
Experimental results for the 14SX experiment series on single-crystal ice supplied by IRL with constrained ends.

Test number	Striker bar velocity (m/s)	Average strain-rate (s^{-1})	Peak stress (MPa)	Strain at peak stress ($\times 10^{-3}$)	Time at peak stress (μs)
14SX-02	5.3	318	14.7	2.6	24.0
14SX-03	3.9	200	21.8	8.1	55.8
14SX-06	3.5	139	17.3	4.8	52.5
14SX-07	3.3	187	10.8	3.9	36.2
14SX-09	5.2	278	24.0	4.4	31.2
14SX-18	3.3	80	19.0	3.9	56.6

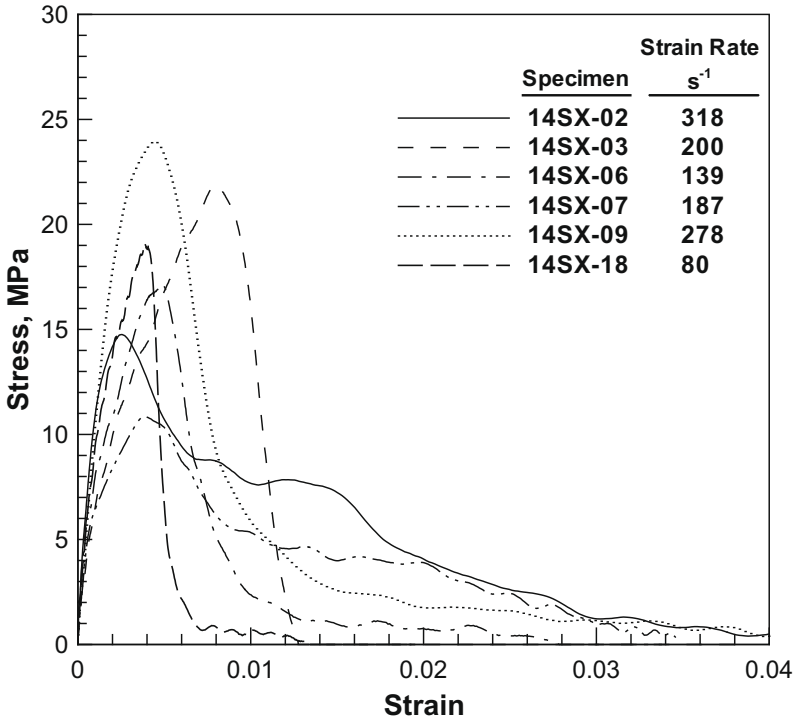

Fig. 14. Stress–strain curves at different strain rates for the 14SX experiment series single-crystal specimens with constrained ends.

in their report, and so a judgment on uniform deformation conditions within the specimens cannot be made with certainty. It should be noted that the values (6.53 MPa) obtained in their quasi-static tests agree well with the static strengths determined by Schulson et al. (2005). Surprisingly, strains corresponding to the peak stress under dynamic loading were less than 2×10^{-3}, as indicated in the representative stress versus strain diagrams of the SHPB experiments (though no values were tabulated as the quasi-static experiments). These values, however, follow the trend of the dependency of strain (at peak stress) on the specimen thickness in the present study, as shown in Fig. 16.

The log–log plot in Fig. 17 gives a more conventional look at the strain-rate effects on ice for experiments conducted at −10 °C. Included in the plot are the data from the present work as well as the

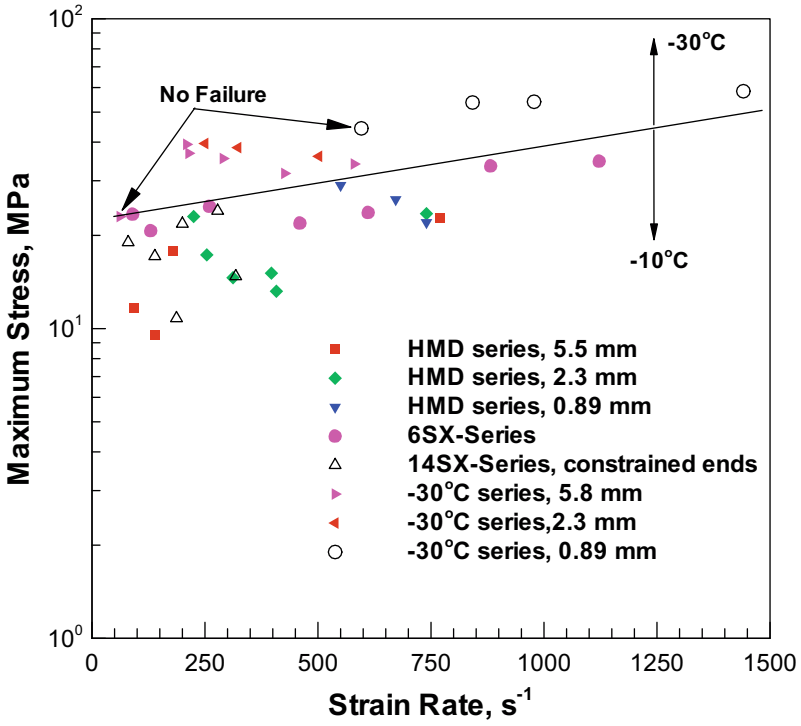

Fig. 15. SHPB results on failure stress- vs. strain-rate of ice in the present study.

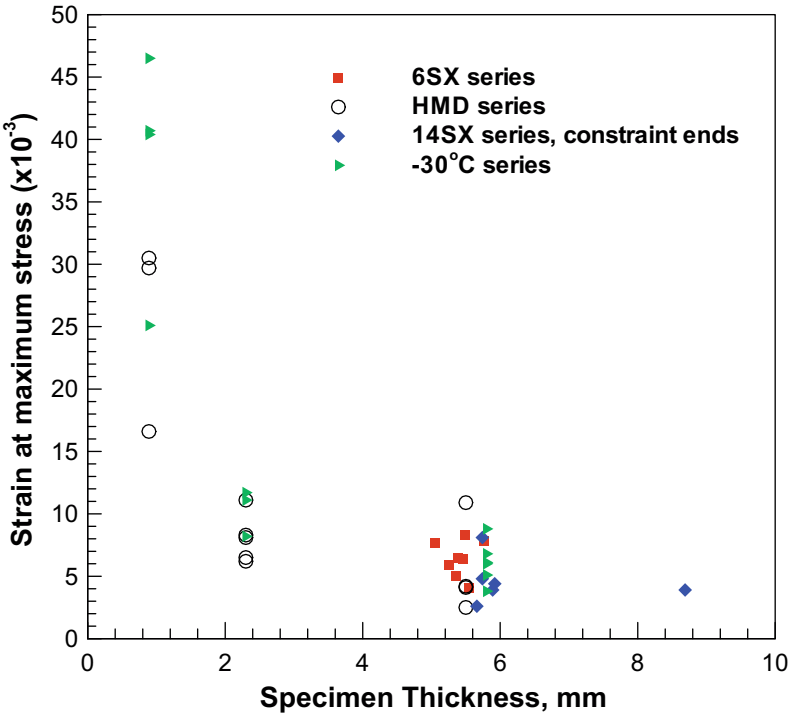

Fig. 16. Variation of strain at peak stress versus specimen thickness.

quasi-static data from Schulson et al. (2005). The plot shows clear, positive strain-rate dependence of peak stress of ice over the strain-rate range of 0.01–1400 s^{-1} (over 5 orders of magnitude). There are two lines plotted in this figure to represent this relationship. The dashed-line represents the regression taken on the quasi-static data only (Schulson et al., 2005) and extrapolated to the higher strain rates. This line over-predicts the peak strength at higher strain rates. A better fit is given by the dashed-dot-dot line, which uses only the polycrystalline data over all strain rates (HMD series in present work). The equation is similar to that given by Schulson et al. (2005) and Jones (1997), and has the higher degree of correlation (R^2 = 0.737). The line is continuous with no jogs. Jones (1997) had previously reported a jogged line as shown as the dashed-line in Fig. 17. Thus, the peak strength of ice has a steady increase with increasing strain-rate, and the relation given by the solid-line is preferred. This behavior also provides more confidence in extrapolating this relationship to still higher strain-rates.

Schulson et al. (2005) have shown a strong relationship of microstructure on the peak strength. In their work single-crystal ice was found to be the strongest, followed by columnar-grained polycrystals, followed by columnar grains loaded at an angle to the columns. While the difference in strength is not as large at the high strain-rates, there is still evidence of stratification, as can be seen in Fig. 15. The single-crystal samples are slightly stronger than the polycrystalline ice samples. A more systematic study is needed to better define this effect.

One important consequence of the results involves the post-peak stress behavior of the impacted ice, in that the sample does not catastrophically lose its load carrying capacity after the attainment of the peak stress. This residual "tail strength" is

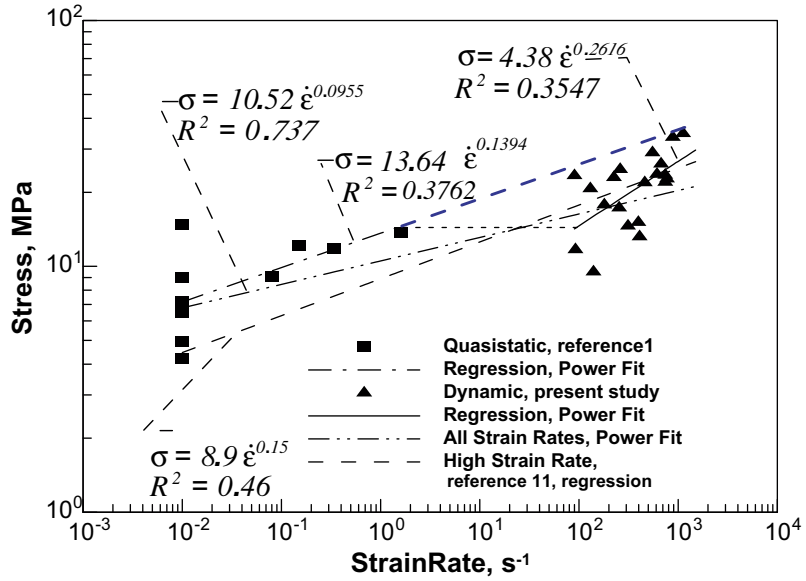

Fig. 17. Comparison of strain rate effects in ice at different strain rate regimes.

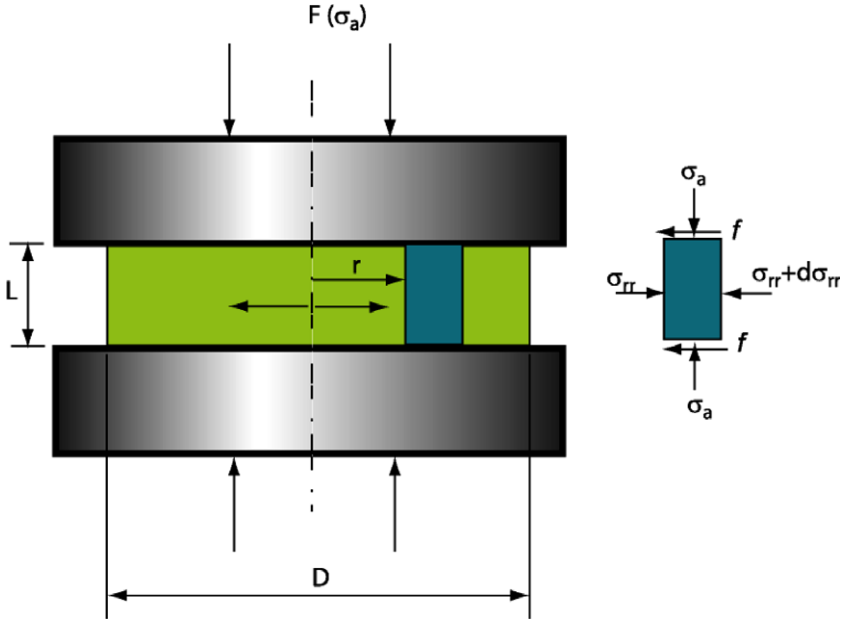

Fig. 18. Schematic of compression test and the forces acting on a material element.

dependent on the sample thickness and strain rate, being higher for thinner samples and larger strain-rates. This is probably because the shards of ice, for the case of thinner specimens, are constrained from falling out of the load train and continue carrying the load. Similar behavior has been observed in drop tower tests at NASA-LaRC and impact tests at NASA GRC (Carney et al., 2006). In these tests, the ice projectiles are observed to completely fragment upon impact, but still continue to impart a sizeable load due to the continued momentum of the ice particles. In fact, in the ballistic ice model used for NASA's "Return-to-flight", the ice impact is treated first as a solid and then as a fluid to account for this continued momentum transfer.

Since the ice samples used in the present study are relatively thin when compared to their diameter, there are concerns that frictional effects at the sample/bar ends could constrain the radial displacement in the sample during loading (ASTM Standard E9, 2000). However, in the experiments conducted in the present study, these effects are believed to be negligible since frictional resistance between ice and the aluminum inserts is minimal at the high sliding rates present in the experiments.

The analysis of uniform uniaxial compression of solid cylinders under the presence of frictional forces, Fig. 18, shows that the radial stress, σ_{rr}, is given by (Kuhn, 2000)

$$\sigma_{rr} = f\frac{D}{L}\left(1-\frac{2r}{D}\right), \tag{5}$$

where f is the frictional stress and is assumed to be constant across the cross-sectional area of the specimen. In general, the radial stress σ_{rr} can be minimized by decreasing the frictional stresses and/or the ratio D/L. Recent experiments on the frictional behavior of ice against various materials (Kennedy et al., 2000; Maeno et al., 2003; Maeno and Arakawa, 2004) showed that the coefficient of kinetic friction is reduced by a factor of 10 as the sliding velocity increases from 10^{-5} to 0.1 m/s. For the SHPB tests, assuming constant volume deformation, the radial velocity of the outside radius of the ice specimen is given by

$$\frac{dr(t)}{dt} = \frac{r_i\dot{\varepsilon}(t)}{(1-\varepsilon(t))^{3/2}}, \tag{6}$$

where r_i is the initial outside diameter, and ε and $\dot{\varepsilon}$ are the instantaneous average strain- and strain-rates in the specimen, respectively. For the case of the experiment conducted at the lowest strain-rate, i.e., 62 s^{-1}, and with an initial diameter of the specimen of ~19.0 mm, the radial component of the particle velocity at the outside diameter of the specimen at the peak stress is approximately 0.6 m/s. This velocity is expected to reduce the coefficient of kinetic friction of ice from approximately 0.06 (Maeno et al., 2003) by a factor of 10, thus negating any effects of friction.

As suggested in Fig. 15, the presence of the end-constraint at the specimen–bar interface has a negligible effect on the measured dynamic failure strength of ice. This is, however, contradictory to that observed in quasi-static compression experiments (Schulson et al., 1999; Schulson et al., 2005), where ends constrained were understood to affect both the mechanical strength and the failure modes of the ice samples. A possible explanation for this behavior could be attributed to the rupture of the interface between the ice disk and the bars in the early stages of loading, followed by a sharp drop in the coefficient of friction with an increase in interfacial sliding speed at the specimen–bar interface. However, more work is still needed to explore this effect completely.

Acknowledgements

The authors acknowledge financial support from NASA Glenn Research Center under contract # NASA – NNC05VA03P. The authors also thank Prof. E.M. Schulson and the Ice Research Laboratory at Dartmouth College, Hanover, NH, for providing ice samples, micro-structural analysis of the ice specimens, and many helpful discussions. Funding for the high-speed camera was provided by NSF's Major Research Instrumentation program through award No.CMS 0079458.

References

Standard Test Methods of Compression Testing of Metallic Materials at Room Temperature – ASTM Designation E9-89a, American Society for Testing and Materials Annual Book of Standards. ASTM International, vol. 03.01, West Conshohocken, PA, 2000, pp. 110–118.

Carney, K.S., Benson, D.J., DuBois, P., Lee, R., 2006. A phenomenological high strain rate model with failure for ice. International Journal of Solids and Structures 43 (25-26), 7820–7839.

Carter, D., 1971. Lois et M'ecanismes de l'apparente Fracture Fragile de la glace de Rivi'ere et de Lac. Ph.D. Dissertation, Universit'e Laval.

Chen, W., 1995. Dyamic failure behavior of ceramics under multiaxial compression. Ph.D. Dissertation, California Institute of Technology.

Cole, D.M., 2001. The microstructure of ice and its influence on mechanical properties. Engineering Fracture Mechanics 68 (17–18), 1797–1822.

Currier, J.H., Schulson, E.M., 1982. The tensile-strength of ice as a function of grain-size. Acta Metallurgica 30 (8), 1511–1514.

Davies, E.D.H., Hunter, S.C., 1963. The dynamic compression testing of solids by the method of the split Hopkinson pressure bar. Journal of the Mechanics and Physics of Solids 11, 155–179.

Dempsey, J.P., Adamson, R.M., Mulmule, S.V., 1999a. Scale effects on the in-situ tensile strength and fracture of ice. Part II: First-year sea ice at Resolute, NWT. International Journal of Fracture 95 (1-4), 347–366.

Dempsey, J.P., Defranco, S.J., Adamson, R.M., Mulmule, S.V., 1999b. Scale effects on the in-situ tensile strength and fracture of ice. Part I: Large grained freshwater ice at Spray Lakes Reservoir, Alberta. International Journal of fracture 95 (1–4), 325–345.

Dutta, P.K., 1993. Compressive failure of polycrystalline ice under impact. In: Proceedings of the Third International Offshore and Polar Engineering Conference, pp. 573–580.

Dutta, P.K., Cole, D.M., Schulson, E.M., Sodhi, D.S., 2003. A fracture study of ice under high strain rate loading. In: Proceedings of the Thirteenth International Offshore and Polar Engineering Conference, pp. 465–472.

Dutta, P.K., Cole, D.M., Schulson, E.M., Sodhi, D.S., 2004. A fracture study of ice under high strain rate loading. International Journal of Offshore and Polar Engineering 14, 182–188.

Frew, D., Forrestal, M., Chen, W., 2002. Pulse shaping techniques for testing brittle materials with a split Hopkinson pressure bar. Experimental Mechanics 42 (1), 93–106.

Haynes, F.D., 1978. Effect of temperature on the strength of snow-ice. CRREL-78-27.

Jones, S.J., 1997. High strain-rate compression tests on ice. Journal of Physical Chemistry B 101 (32), 6099–6101.

Jones, S.J., 2007. A review of the strength of iceberg and other freshwater ice and the effect of temperature. Cold Regions Science and Technology 47, 256–262.

Kennedy, F.E., Schulson, E.M., Jones, D.E., 2000. The friction of ice on ice at low sliding velocities. Philosophical Magazine A 80 (5), 1093–1110.

Kim, H., Kedward, K.T., 2000. Modeling hail ice impacts and predicting impact damage initiation in composite structures. AIAA Journal 38 (7), 1278–1288.

Kim, H., Keune, J.N., 2007. Compressive strength of ice at impact strain rates. Journal of Materials Science 42, 2006–2802.

Kim, H., Welch, D.A., Kedward, K.T., 2003. Experimental investigation of high velocity ice impacts on woven carbon/epoxy composite panels. Composites, Part A 34 (1), 25–41.

Kuhn, H.A., 2000. Universal compression testing. In: Mechanical Testing and Evaluation, ASM Handbook, tenth ed. vol. 8. ASM International, Materials Park, OH, pp. 143–151.

Maeno, N., Arakawa, M., 2004. Adhesion shear theory of ice friction at low sliding velocities, combined with ice sintering. Journal of Applied Physics 95 (1), 134–139.

Maeno, N., Arakawa, M., Yasutome, A., Mizukami, N., Kanazawa, S., 2003. Ice–ice friction measurements, and water lubrication and adhesion-shear mechanisms. Canadian Journal of Physics 81 (1-2), 241–249.

Nixon, W.A., Schulson, E.M., 1987. A micromechanical view of the fracture-toughness of ice. Journal De Physique, Colloque C1 48, 313–319.

Petrovic, J.J., 2003. Mechanical properties of ice and snow. Journal of Materials Science 38 (1), 1–6.

Rigsby, G.P., 1951. Crystal fabric studies on Emmons glacier, Mount Rainer, Washington. Journal of Geology 49, 590–598.

Sarva, S., Nemat-Nasser, S., 2001. Dynamic compressive strength of silicon carbide under uniaxial compression. Materials Science and Engineering A 317 (1–2), 140–144.

Schulson, E.M., 1990. The brittle compressive fracture of ice. Acta Metallurgica et Materialia 38 (10), 1963–1976.

Schulson, E.M., 1999. The structure and mechanical behavior of ice. Journal of the Minerals Metals & Materials Society 51 (2), 21–27.

Schulson, E.M., 2001. Brittle failure of ice. Engineering Fracture Mechanics 68 (17–18), 1839–1887.

Schulson, E.M., Iliescu, D., Renshaw, C.E., 1999. On the initiation of shear faults during brittle compressive failure: a new mechanism. Journal of Geophysical Research-Solid Earth 104 (B1), 695–705.

Schulson, E.M., Iliescu, D., Frott, A., 2005. Characterization of ice for return-to-flight of the space shuttle. Part 1 – Hard ice. NASA CR-2005-213643-Part 1.

Shan, R.L., Jiang, Y.S., Li, B.Q., 2000. Obtaining dynamic complete stress–strain curves for rock using the split Hopkinson pressure bar technique. International Journal of Rock Mechanics and Mining Sciences 37 (6), 983–992.

Shazly, M., Prakash, V., Lerch, B.A., 2005. High strain rate compression testing of ice, Paper # 318 (s14). In: Proceedings of the 2005 SEM Annual Conference and Exposition on Experimental and Applied Mechanics. Society of Experimental Mechanics, Bethel, CT, USA, Portland, Oregon, USA, pp. 359–365.

Shazly, M., Prakash, V., Lerch, B., 2006. High strain-rate compression of ice. NASA Glenn Research Center. E-15282; NASA TM-2006-213966, 95 pp.

Sherburn, J.A. 2007. Hydrodynamic Modeling of Impact Craters. Ms Thesis, Mississippi State University, Starkville.

St. John, J.W., Daley, C.G., 1984. Shipboard measurements of ice pressures in the Bering, Chukchi and Beauforts Seas. In: Proceedings of the International offshore Mechanics and Arctic Engineering Symposium, pp. 260–266.

Sunny, G.P., Lewandowski, J.J., Prakash, V., 2007. Effects of annealing and specimen geometry on dynamic compression of a zirconium-based bulk metallic glass. Journal of Materials Research 22 (2), 389–401.

Uchida, T., Kusumoto, S., 1999. Effects of test conditions on fracture toughness and fracture morphology of polycrystalline ice. JSME International Journal, Series A 42 (4), 601–609.

Weber, L.J., Nixon, W.A., 1996. Fracture toughness of freshwater ice. 1. Experimental technique and results. Journal of Offshore Mechanics and Arctic Engineering-Transactions of the ASME 118 (2), 135–140.